Hydrol. Earth Syst. Sci. Discuss., 12, 8891–8925, 2015
www.hydrol-earth-syst-sci-discuss.net/12/8891/2015/
doi:10.5194/hessd-12-8891-2015

Hydrology and Earth System Sciences
Open Access
Discussions

Estimation of deep infiltration in unsaturated limestone environments using cave LiDAR and drip count data

K. Mahmud[1], G. Mariethoz[2], A. Baker[1], P. C. Treble[3], M. Markowska[1,3], and E. McGuire[4]

[1]Connected Waters Initiative Research Centre, UNSW Australia, Sydney, Australia
[2]Institute of Earth Surface Dynamics, University of Lausanne, Lausanne, Switzerland
[3]Institute for Environmental Research, Australian Nuclear Science and Technology Organisation, Lucas Heights, Sydney, Australia
[4]Department of Parks and Wildlife, Busselton, Western Australia, Australia

Received: 12 August 2015 – Accepted: 14 August 2015 – Published: 2 September 2015

Correspondence to: K. Mahmud (kashif.mahmud@unsw.edu.au)

Published by Copernicus Publications on behalf of the European Geosciences Union.

Abstract

Limestone aeolianites constitute karstic aquifers covering much of the western and southern Australian coastal fringe. They are a key groundwater resource for a range of industries such as winery and tourism, and provide important ecosystem services such as habitat for stygofauna. Moreover, recharge estimation is important for understanding the water cycle, for contaminant transport, for water management and for stalagmite-based paleoclimate reconstructions. Caves offer a natural inception point to observe both the long-term groundwater recharge and the preferential movement of water through the unsaturated zone of such limestone. With the availability of automated drip rate logging systems and remote sensing techniques, it is now possible to deploy the combination of these methods for larger scale studies of infiltration processes within a cave. In this study, we utilize a spatial survey of automated cave drip monitoring in two large chambers of the Golgotha Cave, South-West Western Australia (SWWA), with the aim of better understanding infiltration water movement and the relationship between infiltration, stalactite morphology and unsaturated zone recharge. By applying morphological analysis of ceiling features from Terrestrial LiDAR (T-LiDAR) data, coupled with drip time series and climate data from 2012–2014, we demonstrate the nature of the relationships between infiltration through fractures in the limestone and unsaturated zone recharge. Similarities between drip-rate time series are interpreted in terms of flow patterns, cave chamber morphology and lithology. Moreover, we develop a new technique to estimate recharge in large scale caves, engaging flow classification to determine the cave ceiling area covered by each flow category and drip data for the entire observation period, to calculate the total volume of cave discharge. This new technique can be applied to other cave sites to identify highly focused areas of recharge and can help to better estimate the total recharge volume.

HESSD
12, 8891–8925, 2015

1 Introduction

Karstic aquifers represent substantial global groundwater resources (Worthington and Gunn, 2009). However, the phenomena related to water movement in the unsaturated zone of karstic systems are not yet fully understood. To better manage karst resources, it is important to understand and predict how water flows in karstified limestone. Many traditional methods developed for constraining groundwater flow regimes in highly heterogeneous karstic aquifers are focussed on the faster drainage components i.e. conduits and channels (Morales et al., 2007, 2010; Pardo-Iguzquiza et al., 2011; Smith et al., 2012). However, these methods are less suitable in characterising water movement through the smaller fracture or matrix flow components of the unsaturated zone, lacking vital information relevant to the complete understanding of flow through fractured rocks.

Recharge estimation is critical for understanding the water cycle, contaminant transport, and for water management. However, monitoring water in the unsaturated zone, especially in highly heterogeneous limestone formations is difficult and estimating recharge is one of the most complicated tasks in the hydrological cycle (Scanlon, 2013). Continuous water content measurement using Time Domain Reflectometry (TDR) (Rimon et al., 2007; Dahan et al., 2007) or neutron activation (Koons and Helmke, 1978; Sophocleous, 1991) allow point study on the unsaturated zone water infiltration rate. Tracers such as fluorescent dyes and environmental isotopes in the unsaturated zone at many sites showed an order of magnitude range in recharge rates over 7–70 m yr^{-1}. This has been attributed to different flow systems (quick flow and slow flow), arid versus humid climate forcing, and variations in storage in the soil and epikarst, e.g. Mendip Hills, England (Friederich and Smart, 1982), Israel (Even et al., 1986), Niaux, France (Bakalowicz and Jusserand, 1987), Pennine karst, England (Bottrell and Atkinson, 1992), Slovenia (Kogovšek, 1997), and Mt Carmel, Israel (Arbel et al., 2008).

HESSD
12, 8891–8925, 2015

At the scale of cave drip waters, studies in geologically-old, fractured limestone (that has undergone past diagenesis) have identified the importance of fracture flow and storage in solutionally enhanced fractures or caves. Matrix storage is also possible in geologically-young limestone that has not undergone past diagenesis and contains primary porosity. Cave drip waters are fed directly from the karst bedrock and overlying soil (White, 2002; Tooth and Fairchild, 2003; Atkinson, 1977; Ford and Williams, 2007; Raesi and Karami, 1997), and variations in the size and orientation of fractures, together with variable storage capacity, play fundamental roles in governing the response of a drip site to individual recharge events (Baker and Brunsdon, 2003). High secondary porosity is associated with the epikarst, a zone of heavily weathered carbonate rock, which may act as a water storage reservoir retarding flow and sustaining slow percolation through the unsaturated zone in rocks where karstification has occurred (Arbel et al., 2010; Williams, 1983).

Drip discharges have been categorized in terms of the type of flow process occurring between recharge water and drip water. One possibility is that the drip water is transported via direct delivery of recharge along preferential flow paths (e.g. fractures). Another one is piston flow, where stored water is expelled from pores and fissures by incoming infiltration water (Baker et al., 2000; Tooth and Fairchild, 2003). A more refined understanding of karst infiltration has been achieved through the use of continuously recording (automated) drip measurement devices, which are capable of resolving fine temporal changes in drip rate (McDonald and Drysdale, 2007). Studies incorporating such measurements have increased our knowledge of seepage dynamics. For example, Markowska et al. (2015) classified five different drip types at Harrie Wood Cave in SE Australia, suggesting the heterogeneous flow in the unsaturated zone due to the nature of the karst architecture. Jex et al. (2012) classified drip behaviour using high-resolution drip time series and employed multi-dimensional scaling (MDS) analyses to cluster the data accordingly. Studies using automated counters have also discovered the role of atmospheric pressure on drip variation, and questioned the linearity

HESSD
12, 8891–8925, 2015

of recharge–discharge response at various time-scales (Genty and Deflandre, 1998; Baker and Brunsdon, 2003).

Caves offer a natural inception point to observe both the long-term recharge and the preferential movement of water through the unsaturated zone of such fractured bedrock by monitoring stalactite drip rates. With the availability of both new drip rate logging systems and remote sensing techniques, it is now possible to deploy the combination of these new measurement methods for larger scale studies of many individual drips within a cave. The goal of this paper is to demonstrate the nature of the relationship between flow types classified by the morphological analysis of stalactites Mahmud et al. (2015) and drip time series characteristics. A spatial survey of automated cave drip monitoring in two large chambers of Golgotha Cave, South-West Western Australia (SWWA), is utilized to achieve this goal. Recharge into the cave is quantified based on the drip data, Terrestrial LiDAR (T-LiDAR) measurements and flow classification. We estimate the water balance to develop a simple model describing the ground surface extent from which flow is focussed on the monitored cave ceiling area and the associated lateral flow within the Tamala limestone formation.

2 Site description

Our study site, Golgotha Cave (36.10° S; 115.05° E, Fig. 1a), is developed in the Spearwood System of the Tamala limestone, which comprises medium to coarse-grained Quaternary calcarenites of predominantly aeolian origin. The limestone is wind-blown calcareous sands that have deposited widely around the western and southern coasts of Australia. The cave chamber was formed by unsaturated zone water flow and subsequent widening by ceiling collapse. The cave is 200 m long and up to 25 m wide, and the limestone bed is 20–30 m thick over the cave (Fig. 1b). The surface vegetation is wet eucalypt forest with a substrate of weathered siliceous dune sands of variable thickness having depths varying from 0.3 and 3 m (Treble et al., 2013). There is mini-

HESSD
12, 8891–8925, 2015

mal surface runoff possibility given the high permeability of the sand layer and thereby maximum potential for infiltration through the karstified limestone.

SWWA has a Mediterranean-type climate, with dry summers and wet winters associated with the seasonal migration of the mid-latitude westerly winds. Rainfall, recorded since 1926 at Forest Grove is 1136.8 ± 184 mm annually (BoM, 2015) (34.07° S; 115.10° E, weather station number 9547, 5 km from the site; Fig. 1a). Typically, the highest rainfall starts in late autumn (May) and carries on during the entire southern hemisphere winter wet period (May–October) (median monthly rainfall is approx. 100 mm) (Fig. 2a). Mean maximum daily temperatures range from 16 °C in July to 27 °C in February. Moisture is delivered by troughs embedded in the westerly flow, but may be sourced from regions to the SW or NW of our site (Bates et al., 2008; Fischer and Treble, 2008). Recorded monthly rainfall conditions are shown in Fig. 2a, for hydrological years 2012, 2013 and 2014, starting from April when the water budget is close to zero. Each hydrological year has a similar pattern during the dry period, with months from October to April showing a water deficit or only a negligible amount of recharge (Fig. 2b). In contrast, there is significant amount of excess water available to infiltrate during the wet season. Hydrological year 2014 was rather dry having 943.8 mm precipitation, far below the long-term annual mean precipitation (1141 mm). Year 2013 was relatively wet (1239.8 mm), whereas 2012 (1008.6 mm) was slightly below the long-term annual mean.

Cumulative water budgets are calculated using precipitation (P) and modelled evapotranspiration (ET) data from the Australian Water Availability Project (AWAP) (Raupach et al., 2009) in order to obtain the total infiltration in the karstic aquifer for each hydrological year. Surface runoff is assumed to be zero given the high permeability of the sand layer over the karst formation. Monthly calculated evapotranspiration is subtracted from the monthly rainfall totals to determine the water budget (i.e. P-ET) shown in Fig. 2b. Potential infiltration is then calculated from all positive monthly water budgets (monthly excess water). The total sum of all monthly excess water for a hydrological year (from April to March the following year) gives the potential infiltration for that par-

HESSD
12, 8891–8925, 2015

ticular year. We calculate an average annual potential infiltration of 696.3 mm during three observed hydrological years, ranging from a minimum of 608.6 mm in 2014 to a maximum of 858.7 mm in 2013.

We installed 34 drip water monitoring sites in the wettest areas of two large chambers of the cave (Fig. 1b) named LiDAR 1 (i.e. sampling area 1, located approx. 60 m into the cave) and LiDAR 2 (i.e. sampling area 2, located approx. 90 m into the cave). Fig. 3 shows the studied ceiling area above the loggers in each chamber. The notation used for site identification consists of a numerical number and a letter/roman number. The first numerical number indicates the chamber and the following letter/roman number indicates a certain drip site within the given chamber. In the second position, a letter/roman number is assigned to distinguish between drip data collection process: the letters specify the sites having both manual and automatic drip counts, and the sites with roman numbers only have drip logger data. In each chamber, the drip loggers were laid out in rough transects approximately following the ceiling gradient. In Chamber 1, sites 1A, 1B, 1i, 1ii, 1iii, 1iv and 1v are underneath the north side of the ceiling with slightly thinner limestone overburden (32 m thick), compared to the south side (32.6 m overburden) where drip loggers 1vi to 1xi were placed (Fig. 3a). This variation in overburden thickness within chamber 1 represents an overall 0.6 m lowering in ceiling elevation from the north to the south side. This slight variation in ceiling elevation means that a higher hydraulic gradient occurs at the south patch that is more densely decorated with stalactites. In chamber 2, the sites are spread over a larger area. The south portion is close to the intersection of the ceiling with the cave wall, having comparatively low ceiling elevation and high overburden thickness. On the other hand, the north side of Fig. 3b is far away from the wall. Site 2E is located in the wettest area, close to the lowest point at which the ceiling and wall intersect, whilst 2B is ~ 5 m from the wall and 2A is ~ 10 m from the wall.

HESSD
12, 8891–8925, 2015

3 Background on flow type classification

Literature suggests that karst hydrological flow properties can be identified from the geometry of stalactites and other morphological features in relation to the cave ceiling (Fairchild and Baker, 2012). Based on this concept, Mahmud et al. (2015) used T-LiDAR measurement to image a cave ceiling including individual stalactites. Statistical and morphological analyses of the point clouds produced by T-LiDAR were then used to categorize the ceiling features into different flow types. Through this analysis, the role of the type of water flow processes was analysed by studying the spatial distribution of a large population of stalactites and their geometric properties (length and aspect ratio) in three sites within the Golgotha Cave system.

Based on the typical types of porosity and infiltration processes in karst, Mahmud et al. (2015) defined three categories of flow for the observed ceiling morphological features. The first category is defined as matrix flow, predominantly driven by the process of water seeping through the rock matrix forming icicle and soda-straw stalactites. The second category is characterized by fracture flow, where water in the fracture openings typically forms curtain-shape stalactites or groups of stalactites aligned in the direction of fracturing. The third flow category is a combination of conduit, fracture and matrix flow, which typically forms circular ceiling features. In this case a combination of different processes can occur, for example when conduits are the result of preferential calcite dissolution along pre-existing fractures, or if the base of the pipe conduit is closed, resulting in a stalactite cluster. The formation of combined flow networks is the key phenomenon that separates karst aquifers from porous and fractured-rock aquifers.

Mahmud et al. (2015) determined that chamber 1 is controlled by matrix flow pattern characterized by icicle-shape and soda straw stalactites that are widely distributed in the roof of chamber 1 (Fig. 3a). Within such a system, infiltration rates are directly proportional to the matrix permeability representing the primary porosity of the karst formation. Hence rates of change of water movement are expected to be low, with slow drip rates of low variability (Fairchild and Baker, 2012). The stalactite pattern in

HESSD
12, 8891–8925, 2015

the ceiling of chamber 2 is shown in Fig. 3b. Morphological analysis of Mahmud et al. (2015) showed that this chamber is likely to be controlled by fracture and combined flow hence drip rates are expected to vary over time in this chamber, depending on water transport in the preferential flow system.

4 Data acquisition and pre-processing

We investigate the relationship between infiltration through the fractured limestone and cave drip water discharge using the morphological analysis of ceiling features, coupled with drip logger and climate data from 2012 to 2014. In this paper, we locate the individual stalactites feeding the drip loggers using T-LiDAR images and digital photos, and identify each as matrix (soda straw or icicle), fracture or combined-flow. These morphology-based classifications are compared with flow characteristics from the drip loggers time series. The discharge from each stalactite is calculated and used to estimate the total discharge over each studied area. The total discharge from each area is compared with infiltration estimates to better understand flow from the surface to the cave ceiling of the studied area.

4.1 T-LiDAR and elevation data

Ground-based T-LiDAR is a commonly used remote sensing technology that records high-resolution 3-dimensional point clouds of the Earth's surface and its use in geology has been growing in recent years (Pringle et al., 2006; Fabuel-Perez et al., 2009; Rotevatn et al., 2009; Wilson et al., 2009). However, karstic model development using T-LiDAR is a novel application. There are few studies that discuss the benefits and the use of this tool, as well as the methods needed to work with this kind of technology (exceptions are (Kaul et al., 2015; Zlot and Bosse, 2014a, b). The T-LiDAR measurements were taken adjacent to two locations where cave drip waters have been sampled for drip rate and chemistry for the past ten years (2005–2014) (Treble et al., 2013, 2015). T-

HESSD
12, 8891–8925, 2015

LiDAR positions 1 and 2 (Fig. 1) were selected such as to cover the significant portions of the ceiling from a perspective close to vertical in order to capture all 34 stalactites feeding the drip loggers while minimizing the occlusion of other stalactites further away from the scanner line-of-sight. Fig. 3 shows scan images for both chambers.

The elevation of the cave floor at the gate is 72 m above sea level (a.s.l.) according to GPS measurements. Elevations of the drip loggers inside the cave were obtained by a cave survey using a fibre surveyors tape as well as a SUUNTO tandem 360PC/360R clinometer to calculate dip and orientation (estimated error for dip is ±1–2° and for orientation is ±5°). A metal surveyors tape was used to measure distance (accuracy ± 0.1 m). Ceiling heights were surveyed from the T-LiDAR data that consist of both the drip logger sites and the ceiling features (i.e. stalactites). A detailed surface survey was performed to gain surface elevation and an estimate of the total thickness of overburden over the cave. A Bosch GLR225 Laser Distance Measurer was also used to measure the distance between points (accuracy ± 1.5 mm).

4.2 Alignment of drip loggers and stalactites

To build the relationship between the flow patterns classified in Mahmud et al. (2015) and the drip time series characteristics, we initially start pairing the individual stalactites feeding the drip with the loggers time series. As an initial processing step, we locate all 34 stalactites in the T-LiDAR images. Close-up images from the ceiling areas were analysed to identify the exact stalactite locations by comparing T-LiDAR images, digital photos and on-site observations. Fig. 3 shows the studied ceiling area of both chambers captured using a T-LiDAR, with stalactite locations identified in blue circles. The stalactites (in short Stal) are named according to the drip loggers' site (e.g. Stal 1A feeds the logger site 1A, and so on). Points (1, 2, 3, 4, 5) are assigned to some significant ceiling features (for example larger stalactites) to register the locations in the T-LiDAR images, digital photos and on-site within the cave (Fig. 3).

HESSD
12, 8891–8925, 2015

4.3 Drip logger data

Automatic drip monitoring sites were established in August 2012. Stalagmate drip loggers (www.driptych.com) were installed throughout the two large chambers (Fig. 1). Data loggers were set to record the number of drops that fell on the logger per 15 min. Data was downloaded at regular intervals of six months, between October 2012 and March 2015, and data collection is ongoing.

Preliminary screening of all drip time series was performed for quality assurance. Based on the initial data screening, we entirely discard five drip sites i.e. 1iv, 1vii, 1xii, 2ii and 2xii. Drips 1iv, 2ii and 2xii show sudden changes in drip rate that likely reflect the logger being accidentally moved or misaligned after data downloads. Loggers 1vii and 1xii were discarded due to the recording of dual drips or missing data. The remaining 29 sites are considered in this study, although parts of these time series were discarded where we considered the data unreliable. Data recorded during periods of known fieldwork were removed from the drip rate time series, including 1 day either side of recorded field trip days as standard protocol. Finally, the time series gaps are filled with synthetic data considering the drip statistics and correlation between drip rates.

The resulting drip-rate time series are plotted for both cave chambers and three hydrological years from April 2012 to March 2015 in Fig. 4. Chamber 1 drip loggers show two different groupings in terms of flow rates. However, most chamber 1 drip loggers exhibit a clear response to the 2013 wet winter, presenting peaks at the end of September 2013 (Fig. 4a). On the contrary, chamber 2 drip rates are more variable between sites (Fig. 4b–d). We further divide the chamber 2 time series into three classes based on their flow behavior throughout the three-year study period: (i) static drips with little discernible variation and very low flow rates (Fig. 4b), (ii) medium-variability drips with moderate discharges (Fig. 4c), and (iii) high-variability drips with high discharges (Fig. 4d). Comparing the slow dripping sites from both monitored chambers, we discover a persistent base flow component even during periods of water deficit, which

HESSD
12, 8891–8925, 2015

feeds storage water to the drip site. These monitoring sites (Fig. 4) exhibit a near constant drip rate, with little or no relationship to hydrologically effective precipitation, except for the response to the 2013 wet winter. Nonetheless, there is still considerable variation between these static drips in terms of base flow, magnitude of response, and attenuation.

5 Data analysis and interpretation

5.1 Flow type classification based on LiDAR data

In this section we briefly describe the methodology that was used to investigate different flow patterns classified in Mahmud et al. (2015). The matrix flow category was subdivided into two subclasses: soda straw and icicle-shaped stalactites based on their geometric properties. Soda-straws were defined as having a diameter of less than 10 mm with a length/diameter ratio greater than 8.We use the LiDAR-based morphological analysis to identify individual stalactites and flow classifications (icicle, soda straw, fracture and combined flow) based on the T-LiDAR point-clouds. Fig. 5a shows the topography (in 2-D) of a portion of the ceiling in site 1 classified into the different flow categories. The outcome of this classification is shown in Fig. 5b. Fig. 6 shows a similar analysis for a different ceiling portion of site 1 containing stalactites feeding sites 1ii, 1iii and 1v classified as soda straw (Fig. 5c).

According to the morphological analysis shown in Figs. 5 and 6, stalactites feeding sites 1A, 1B, 1i, 1ii and 1iii are in the icicle flow category, and the stalactite feeding site 1v is classified as soda straw. Similar morphological analyses were performed for all stalactites that feed the loggers in both studied chambers. As a result, we identify that the majority of drip flows from chamber 1 are icicle type, with one possible location for each of soda straw (site 1v), fracture (site 1x) and combined flow (site 1viii). In contrast, drip loggers in chamber 2 are recording a completely different setting, having a variety of flow patterns (9 locations of icicle flow, 4 of fracture flow, 3 of combined flow and

HESSD
12, 8891–8925, 2015

2 soda straws). These results are consistent with field evidence: chamber 1 ceiling is dominated by soda straw and icicle-shape stalactites suggesting matrix flow and stalactites in chamber 2 tend to be more isolated and evolving either along fractures or at the margins of relict dune surfaces (Treble et al., 2013).

5.2 Relation between LiDAR-based classification and drip data

The LiDAR-based flow classification for individual sites is detailed in Table 1 and Table 2. The average drip rates per 15 minutes, skewness, coefficient of variation (COV) and the elevations of cave ceiling at the location of the stalactites are also listed to compare various flow categories. Coefficient of variation (COV) is defined as the ratio of the standard deviation (σ) to the mean (μ). To build up the relationship between LiDAR-based flow classification and drip rates, drip logger mean discharge, skewness and COV are plotted in Fig. 7 against the overburden limestone thickness above all drip sites (from 32.4 to 41.9 m). We observe no significant relationship between the drip logger mean discharge, skewness and COV with overburden thickness, however these properties can be used to characterize different flow classes, and are discussed below in further details.

All chamber 1 icicle flow have slow drips i.e. less than 5 drips every 15 mins (Table 1), resulting mean discharges ranging from 6 to 20 L yr^{-1}. Their drip rates remain almost constant throughout the study period (Fig. 4a). However, it is evident that the drip loggers exhibit a clear response to the 2013 wet winter, with peak discharge at the end of September 2013 (Fig. 4a). Icicle drip discharges in chamber 2 show similar results, with slightly higher drip rates up to 8.5 drips per 15 mins, discharging 42.7 L yr^{-1}. All these icicle flow types display low values of skewness and intermediary variation (COV) within the time series (Fig. 7b and c).

Drip sites classified as soda straws (site 1v, 2iii and 2xi) have usually very low discharges (less than 2 drips per 15 min). However, these drips have large skewness and variation (COV) (Tables 1 and 2 and Fig. 7b). Among these soda straw flows, site 2xi has the lowest mean discharge of 0.5 L yr^{-1} and shows the largest variation (COV)

HESSD
12, 8891–8925, 2015

within the time series (Table 2). Moreover, such soda straw drips do not exhibit constant discharge according to the drip time series (Fig. 4a and b), even though they have extremely low discharges.

Site classified as combined flow type (1viii, 2E, 2v and 2viii) have high discharges ranging from 12 to 28 drips per 15 mins (60–140 L yr^{-1}). In addition, these drips have comparatively extended range of skewness and COV (Fig. 7b and c). Lastly, sites 1x, 2i, 2vi, 2ix and 2xvi, characterized as fracture flows according to the morphological analysis, have typically the largest discharges (Fig. 7a). There is significant variability in discharge between these sites and within the individual time series (Fig. 4), evidenced by differences in mean discharge rates, skewness and coefficient of variation, e.g. mean discharge ranging from 90 to 2700 L s^{-1}.

We compute the correlation matrix between all drip sites (Fig. 8). The different sites are aligned in the matrix according to the flow classification. Various flow types (I = Icicle, F = Fracture, C = Combined, S = Soda straw) characterized by the morphological analysis are shown in parenthesis with the site notation in Fig. 8. The correlation between similar flow types can be visualized from the correlation matrix (Fig. 8). All chamber 1 sites from the north patch representing icicle and soda straw flows (1v, 1A, 1B, 1i, 1ii and 1iii) are highly positively correlated (Fig. 8a). However, sites 1vi, 1ix and 1xi (with icicle flow characteristics and falling within the south patch of chamber 1) do not indicate significant correlations, suggesting spatial dependence on the drip discharge. On the other hand, chamber 2 sites belonging to fracture and combined flow categories show moderate to high positive correlation with each other, possibly being highly responsive to rainfall events (Fig. 8b). All icicle and soda straw flow sites are correlated to each other in a similar fashion, except sites 2A and 2xiii which are negatively correlated with rest of the drip discharges. These two sites show decreasing drip rates while the rest of the sites from chamber 2 have increasing trends, suggesting flow-switching possibility at higher flows/heads.

HESSD
12, 8891–8925, 2015

5.3 Cave discharge estimation

The infiltration of water through the limestone formation within the monitored areas of both chambers is estimated based on the drip data and the T-LiDAR measurements. We consider the drip data for the entire observation period to calculate the total drip counts for each logger and thus obtain the total cave-integrated drip water volume, considering 1 drip = 0.1433 mL according to (Genty and Deflandre, 1998). Using the flow classification of Sect. 5.1, we can determine the area covered by each flow category. Further, we know the average drip discharge for each flow category (Tables 1 and 2), thus potentially allowing us to estimate the total flux volume.

It is clear that not all stalactites are actively dripping, therefore to have an accurate quantification of the total drip flux we need to know the fraction of stalactites that are actively dripping. This is done by looking at a series of the digital photos of the chamber ceiling to determine which stalactites have a water beads on their tip. One single frame from chamber 1 ceiling is shown in Fig. 9. In this ceiling portion, there is a total of 45 stalactites (total red and yellow circles), among which 32 are actively dripping (red circles). Therefore, on this image 71.1 % of the stalactites are active. Similarly, we use other digital images of ceiling areas covering the rest of the monitored sites, and consider the average percentage for each chamber ceiling.

Finally, the total flux (Table 3) for each flow category i is obtained (i.e. $Q_{\text{icicle}}, Q_{\text{fracture}}, Q_{\text{combined}}, Q_{\text{soda-straw}}$) by multiplying the total number of active stalactite for each category (n) with the corresponding measured drip discharge for the corresponding category (q):

$$
\begin{aligned}
Q_{\text{icicle}} &= n_{\text{icicle}} q_{\text{icicle}} \\
Q_{\text{fracture}} &= n_{\text{fracture}} q_{\text{fracture}} \\
Q_{\text{combined}} &= n_{\text{combined}} q_{\text{combined}} \\
Q_{\text{soda-straw}} &= n_{\text{soda-straw}} q_{\text{soda-straw}}
\end{aligned} \tag{1}
$$

HESSD
12, 8891–8925, 2015

The total discharge (Q) is obtained by summing the flux for all categories:

$$Q = Q_{\text{icicle}} = +Q_{\text{fracture}} + Q_{\text{combined}} + Q_{\text{soda-straw}} \quad (2)$$

We predict total cave discharge amount within the monitored ceiling area of both chambers using total drip counts and flow types categorized by the morphological analysis. Table 3 demonstrates the summary for both chambers considering all drip discharges.

We estimate the water balance to understand the extent to which flow is focussed on the cave ceiling and to quantify the associated lateral flow within the Tamala limestone formation (Fig. 10). Monitored ceiling areas are 30.4 and 55.2 m^2 respectively for chamber 1 and 2, though the infiltration water comes from a larger surface area of 36.8 and 92.9 m^2 suggesting that infiltration is being focussed to the studied areas of each chamber, by approximately 120 and 170 % respectively. A portion of this calculation may be the result of uncertainties involved in the methodology such as modelled ET or active stalactite count, but our field observations of the cave ceiling support focussed flow. For example, these studied ceiling areas are dominated by karst water infiltration compared to other ceiling portions consisting of dry and bare rock surface without any stalactite formation. Another possible uncertainty source involves in the process of stalactite identification and flow classification based on the morphological analysis, which controls the amount of measured flow. This is a semi-automated segmentation process where the user controls parameters such as moving average window size and threshold to perform the morphology-based analysis. These parameters are adjusted to the particular cave site and, typically for segmentation procedures, involve a trade-off between over- and under-segmentation (Hyyppa et al., 2001). While the optimal parameters minimize both types of error, there is generally no parameters combination that results in a perfect, error-free segmentation (Mahmud et al., 2015).

The total counts of stalactites identified by morphological analysis in both chambers are around 2000, with chamber 1 being almost twice as densely populated as chamber 2 (Table 3). However, the proportion of active stalactites is higher in chamber 2, with a

HESSD
12, 8891–8925, 2015

larger flux (per m^2) that potentially suggests greater lateral flow dispersion in chamber 2 (Table 3). Moreover, chamber 2 ceiling covers a greater surface area (92.9 m^2), has the relatively lower ceiling elevation and is adjacent to the cave wall (Fig. 10). This points out an influence of hydraulic gradient on water movement in this area. We suggest that this may be indicating that a large portion of infiltrating water is flowing around the cave and inside the ceiling, rather than through it. The cave ceiling may be acting as a capillary barrier resulting in water moving along the ceiling gradient towards the lower eastern wall (Figs. 1 and 10).

6 Conclusion

Cave drip response to unsaturated zone recharge is complex and therefore involves the interaction of several drip pathways with differing response times. This study highlights the importance of hydrogeological controls on water movement in the karst unsaturated zone, which have a critical influence on drip hydrology. The nature of the karst architecture leads to heterogeneous flow in the unsaturated zone, characterized with four different flow types classified using the morphological analysis of Mahmud et al. (2015). This paper applies this method to identify flow types for the individual stalactite discharges measured by continuous hydrological monitoring in a SWWA karst, where hydrological variations are strongly controlled by seasonal variations in recharge. We discover that the discharge data and the morphology-based flow classification agree with each other in terms of flow and geometrical characteristics of ceiling stalactites. We further investigate the drip rates and cave discharge relationship. The mean annual infiltration is found to be 60–70 % of the annual precipitation. Deviations from expected seasonal discharge characteristics have been noted in few drip discharges. Moreover, the slow dripping sites (icicle and soda-straw) show significant drip variations even though having uniform nature of drip profiles, indicating differential pressure heads and substantial flow path variability in the overlying unsaturated zone.

HESSD
12, 8891–8925, 2015

We observe no significant relationships between the drip logger mean discharge, skewness and COV with overburden thickness, due to the possibility of potential unsaturated zone storage volume and increasing complexity of the karst architecture. However, these properties can be used to characterize different flow classes. The correlation matrix shows that similar flow categories are positively correlated, with a significant influence of spatial distribution. We hypothesize that the amount of discharge from chamber 1 monitored area is equal to the unsaturated zone recharge within the area of limestone formation. However, the majority of the cave ceiling portion is dry in our cave site, suggesting the possibility of capillary effect with water moving around the cave rather than passing through it, especially within studied area of chamber 2 that has relatively lower ceiling elevation and is adjacent to the cave wall.

We demonstrate that morphological properties of stalactites and drip rate monitoring is a suitable means by which to classify karst flow behaviour, and should be the focus of future studies using a larger dataset of drip loggers, both temporally and spatially, and a wider range of limestone geologies. At Golgotha Cave, the collection of drip logger data is ongoing, as well as analysis of tracers of water movement such as stable isotopes. These data will be the focus of future research to expand the possibility of classifying geochemical properties of drip regimes covering large-scale observation.

Acknowledgements. This work was supported by a scholarship from UNSW, the Gary Johnston Fund, and the research projects undertaken as part of the Australian Research Council and National Water Commission funding for the National Centre for Groundwater Research and Training (NCGRT). The outcomes of this study contribute to Discovery Project DP140102059 awarded to PCT.

Alan Griffiths, Andy Spate, Anne Wood, are thanked for their assistance in the field and with data access. The Department of Parks and Wildlife (WA) are thanked for their ongoing support to conduct scientific research at Golgotha Cave.

HESSD
12, 8891–8925, 2015

References

Arbel, Y., Greenbaum, N., Lange, J., Shtober-Zisu, N., Grodeck, T., Wittenberg, L., and Inbar, M.: Hydrologic classification of cave drips in a Mediterranean climate, based on hydrograph separation and flow mechanisms, Isr. J. Earth Sci., 57, 291–310, 2008.

Arbel, Y., Greenbaum, N., Lange, J., and Inbar, M.: Infiltration processes and flow rates in developed karst vadose zone using tracers in cave drips, Earth Surf. Proc. Land., 35, 1682–1693, doi:10.1002/esp.2010, 2010.

Atkinson, T. C.: Diffuse flow and conduit flow in limestone terrain in the Mendip Hills, Somerset (Great Britain), J. Hydrol., 35, 93–110, doi:10.1016/0022-1694(77)90079-8, 1977.

Bakalowicz, M. J. and Jusserand, C.: Etude de l'infiltration en milieu karstique par les methodes geochemiques et isotopiques Cas de la Grotte de Niaux, Bulletin du Centre d'Hydrogeologie, 1987, 265–283, 1987.

Baker, A. and Brunsdon, C.: Non-linearities in drip water hydrology: an example from Stump Cross Caverns, Yorkshire, J. Hydrol., 277, 151–163, doi:10.1016/S0022-1694(03)00063-5, 2003.

Baker, A., Genty, D., and Fairchild, I. J.: Hydrological characterisation of stalagmite dripwaters at Grotte de Villars, Dordogne, by the analysis of inorganic species and luminescent organic matter, Hydrol. Earth Syst. Sci., 4, 439–449, doi:10.5194/hess-4-439-2000, 2000.

Bates, B., Hope, P., Ryan, B., Smith, I., and Charles, S.: Key findings from the Indian Ocean Climate Initiative and their impact on policy development in Australia, Climatic Change, 89, 339–354, doi:10.1007/s10584-007-9390-9, 2008.

BoM: Climate Data Online (Station 9547), Bureau of Meteorology Melbourne, http://www.bom.gov.au/climate/data/ (last ccess: 26 August 2014), 2015.

Bottrell, S. H. and Atkinson, T. C.: Tracer study of flow and storage in the unsaturated zone of a karstic limestone aquifer, Tracer Hydrology, edited by: Hotzl, H. and Werner, A., A a Balkema, Rotterdam, 207–211, 1992.

Dahan, O., Shani, Y., Enzel, Y., Yechieli, Y., and Yakirevich, A.: Direct measurements of floodwater infiltration into shallow alluvial aquifers, J. Hydrol., 344, 157–170, doi:10.1016/j.jhydrol.2007.06.033, 2007.

Even, H., Carmi, I., Magaritz, M., and Gerson, R.: Timing the transport of water through the upper vadose zone in a Karstic system above a cave in Israel, Earth Surf. Proc. Land., 11, 181–191, doi:10.1002/esp.3290110208, 1986.

HESSD
12, 8891–8925, 2015

Fabuel-Perez, I., Hodgetts, D., and Redfern, J.: A new approach for outcrop characterization and geostatistical analysis of a low-sinuosity fluvial-dominated succession using digital outcrop models: Upper Triassic Oukaimeden Sandstone Formation, central High Atlas, Morocco, AAPG Bulletin, 93, 795–827, 2009.

Fairchild, I. J. and Baker, A.: Speleothem Science: From Process to Past Environments, Wiley-Blackwell, Chichester, 450 pp., 2012.

Fischer, M. J. and Treble, P. C.: Calibrating climate-δ^{18}O regression models for the interpretation of high-resolution speleothem δ^{18}O time series, J. Geophys. Res.-Atmos., 113, D17103, doi:10.1029/2007jd009694, 2008.

Ford, D. and Williams, P. D.: Karst Hydrogeology and Geomorphology, Wiley, Chichester, 561 pp., 2007.

Friederich, H. and Smart, P. L.: The classification of autogenic percolation waters in karst aquifers: A study in G.B. cave, Mendip Hills, England, Proceedings of the University of Bristol Speleological Society, 1982, 143–159, 1982.

Genty, D. and Deflandre, G.: Drip flow variations under a stalactite of the Pere Noel cave (Belgium), Evidence of seasonal variations and air pressure constraints, J. Hydrol., 211, 208–232, 1998.

Hyyppa, J., Kelle, O., Lehikoinen, M., and Inkinen, M.: A segmentation-based method to retrieve stem volume estimates from 3-D tree height models produced by laser scanners, IEEE T. Geosci. Remote, 39, 969–975, doi:10.1109/36.921414, 2001.

Jex, C. N., Mariethoz, G., Baker, A., Graham, P., Andersen, M., Acworth, I., Edwards, N., and Azcurra, C.: Spatially dense drip hydrological monitoring and infiltration behaviour at the Wellington Caves, South East Australia, Int. J. Speleol., 41, 283–296, 2012.

Kaul, L., Zlot, R., and Bosse, M.: Continuous-Time Three-Dimensional Mapping for Micro Aerial Vehicles with a Passively Actuated Rotating Laser Scanner, J. Field Robot. doi:10.1002/rob.21614, 2015.

Kogovšek, J.: Water tracer tests in the vadose zone, Tracer Hydrology, Balkema, Rotterdam, 1997.

Koons, R. D. and Helmke, P. A.: Neutron Activation Analysis of Standard Soils, Soil Sci. Soc. Am. J., 42, 237–240, doi:10.2136/sssaj1978.03615995004200020004x, 1978.

Mahmud, K., Mariethoz, G., Pauline, C. T., and Baker, A.: Terrestrial Lidar Survey and Morphological Analysis to Identify Infiltration Properties in the Tamala Limestone, Western Australia, IEEE J. Sel. Top. Appl., in press, 2015.

HESSD
12, 8891–8925, 2015

Markowska, M., Baker, A., Treble, P. C., Andersen, M. S., Hankin, S., Jex, C. N., Tadros, C. V., and Roach, R.: Unsaturated zone hydrology and cave drip discharge water response: Implications for speleothem paleoclimate record variability, J. Hydrol., doi:10.1016/j.jhydrol.2014.12.044, in press, 2015.

McDonald, J. and Drysdale, R.: Hydrology of cave drip waters at varying bedrock depths from a karst system in southeastern Australia, Hydrol. Process., 21, 1737–1748, doi:10.1002/hyp.6356, 2007.

Morales, T., Fdez. de Valderrama, I., Uriarte, J. A., Antigüedad, I., and Olazar, M.: Predicting travel times and transport characterization in karst conduits by analyzing tracer-breakthrough curves, J. Hydrol., 334, 183–198, doi:10.1016/j.jhydrol.2006.10.006, 2007.

Morales, T., Uriarte, J. A., Olazar, M., Antigüedad, I., and Angulo, B.: Solute transport modelling in karst conduits with slow zones during different hydrologic conditions, J. Hydrol., 390, 182–189, doi:10.1016/j.jhydrol.2010.06.041, 2010.

Pardo-Iguzquiza, E., Durán-Valsero, J. J., and Rodríguez-Galiano, V.: Morphometric analysis of three-dimensional networks of karst conduits, Geomorphology, 132, 17–28, doi:10.1016/j.geomorph.2011.04.030, 2011.

Pringle, J. K., Howell, J. A., Hodgetts, D., Westerman, A. R., and Hodgson, D. M.: Virtual outcrop models of petroleum reservoir analogues: a review of the current state of-the-art, First Break, 24, 33–42, 2006.

Raesi, E. and Karami, G.: Hydrochemographs of Berghan Karst Springs as indicators of aquifer characteristics, J. Cave Karst Stud., 59, 112–118, 1997.

Raupach, M. R., Briggs, P. R., Haverd, V., King, E. A., Paget, M., and Trudinger, C. M.: Australian Water Availability Project (AWAP): CSIRO Marine and Atmospheric Research Component: Final Report for Phase 3, 67, 2009.

Rimon, Y., Dahan, O., Nativ, R., and Geyer, S.: Water percolation through the deep vadose zone and groundwater recharge: Preliminary results based on a new vadose zone monitoring system, Water Resour. Res., 43, W05402, doi:10.1029/2006wr004855, 2007.

Rotevatn, A., Buckley, S. J., Howell, J. A., and Fossen, H.: Overlapping faults and their effect on fluid flow in different reservoir types: A LIDAR-based outcrop modeling and flow simulation study, AAPG Bulletin, 93, 407–427, 2009.

Scanlon, B. R.: Evaluation of Methods of Estimating Recharge in Semiarid and Arid Regions in the Southwestern U.S, in: Groundwater Recharge in a Desert Environment: The Southwestern United States, American Geophysical Union, 235–254, 2013.

HESSD
12, 8891–8925, 2015

Smith, A. J., Massuel, S., and Pollock, D. W.: Geohydrology of the Tamala Limestone Formation in the Perth Region: Origin and Role of Secondary Porosity, CSIRO: Water for a Healthy Country National Research Flagship, 63 pp., 2012

Sophocleous, M. A.: Combining the soilwater balance and water-level fluctuation methods to estimate natural groundwater recharge: Practical aspects, J. Hydrol., 124, 229–241, doi:10.1016/0022-1694(91)90016-B, 1991.

Tooth, A. F. and Fairchild, I. J.: Soil and karst aquifer hydrological controls on the geochemical evolution of speleothem-forming drip waters, Crag Cave, southwest Ireland, J. Hydrol., 273, 51–68, doi:10.1016/S0022-1694(02)00349-9, 2003.

Treble, P. C., Bradley, C., Wood, A., Baker, A., Jex, C. N., Fairchild, I. J., Gagan, M. K., Cowley, J., and Azcurra, C.: An isotopic and modelling study of flow paths and storage in Quaternary calcarenite, SW Australia: implications for speleothem paleoclimate records, Quaternary Sci. Rev., 64, 90–103, doi:10.1016/j.quascirev.2012.12.015, 2013.

Treble, P. C., Fairchild, I. J., Griffiths, A., Baker, A., Meredith, K. T., Wood, A., and McGuire, E.: Impacts of cave air ventilation and in-cave prior calcite precipitation on Golgotha Cave dripwater chemistry, southwest Australia, Quaternary Sci. Rev., doi:10.1016/j.quascirev.2015.06.001, in press, 2015.

White, W. B.: Karst hydrology: recent developments and open questions, Eng. Geol., 65, 85–105, doi:10.1016/S0013-7952(01)00116-8, 2002.

Williams, P. W.: The role of the subcutaneous zone in karst hydrology, J. Hydrol., 61, 45–67, doi:10.1016/0022-1694(83)90234-2, 1983.

Wilson, P., Hodgetts, D., Rarity, F., Gawthorpe, R. L., and Sharp, I. R.: Structural geology and 4D evolution of a half-graben: New digital outcrop modelling techniques applied to the Nukhul half-graben, Suez rift, Egypt, J. Struct. Geol., 31, 328–345, doi:10.1016/j.jsg.2008.11.013, 2009.

Worthington, S. R. H. and Gunn, J.: Hydrogeology of Carbonate Aquifers: A Short History, Ground Water, 47, 462–467, doi:10.1111/j.1745-6584.2008.00548.x, 2009.

Zlot, R. and Bosse, M.: Three-Dimensional Mobile Mapping of Caves, J. Cave Karst Stud., 76, 191–206, doi:10.4311/2012EX0287, 2014a.

Zlot, R. and Bosse, M.: Efficient Large-scale Three-dimensional Mobile Mapping for Underground Mines, J. Field Robot., 31, 758–779, 2014b.

HESSD
12, 8891–8925, 2015

Table 1. Flow classification of chamber 1 drip data.

Site/Stalagmate	Elevation (a.s.l. m)	Average drip rate per 15 min	T-LiDAR classified flow type	Skewness	Coefficient of variation (COV)
1A	77.46	4.0	Icicle	0.17	18.23
1B	77.424	2.5	Icicle	−0.03	19.93
1i	77.4	1.3	Icicle	0.13	40.31
1ii	77.521	2.2	Icicle	−0.06	28.09
1iii	77.655	1.2	Icicle	−0.29	30.52
1v	77.585	1.3	Soda-straw	1.21	40.83
1vi	77.036	1.5	Icicle	0.1	33.83
1viii	77.167	12.1	Combined	0.38	42.49
1ix	76.88	3.0	Icicle	0.23	21.01
1x	76.9	17.2	Fracture	0.19	28.88
1xi	76.885	2.5	Icicle	−0.71	48.98

HESSD
12, 8891–8925, 2015

Table 2. Flow classification of chamber 2 drip data.

Site/Stalagmate	Elevation (a.s.l. m)	Average drip rate per 15 min	T-LiDAR classified e flow typ	Skewness	Coefficient of variation (COV)
2A	75.48	1.9	Icicle	−0.24	44.31
2B	73.49	3.4	Icicle	0.2	16.01
2E	72.37	27.9	Combined	−0.59	6.21
2i	72.22	48.4	Fracture	0.31	2.57
2iii	75.2	0.8	Soda-straw	−1.64	45.62
2iv	73.7	2.9	Icicle	−0.82	13.23
2v	75.75	13.5	Combined	0.10	8.30
2vi	75.66	196.1	Fracture	0.44	5.65
2vii	75.7	4.1	Icicle	0.03	100.95
2viii	73.72	22.7	Combined	−0.11	21.63
2ix	73.34	71.7	Fracture	−0.22	16.11
2x	73.59	1.4	Icicle	0.5	43.86
2xi	73.5	0.1	Soda-straw	2.68	289.31
2xiii	73.54	5.2	Icicle	−0.47	25.29
2xiv	73.49	8.5	Icicle	−0.17	11.81
2xv	73.36	2.3	Icicle	0.56	21.57
2xvi	73.52	53.8	Fracture	0.17	45.28
2xvii	73.72	1.4	Icicle	−0.06	53.08

HESSD
12, 8891–8925, 2015

Table 3. Cave discharge calculation for both chambers

Parameters	Chamber 1	Chamber 2
Average rainfall (mm yr^{-1})	1106	
Average infiltration (mm yr^{-1})	696.27	
Studied ceiling area (m^2)	30.4 (9.5 m × 3.2 m)	55.2 (8.0 m × 6.9 m)
Total number of stalactites	1909	2023
Density of stalactites per m^2	68	37
Proportion of active Stalactites (%)	57	76
Total flux volume (m^3 yr^{-1})	25.6	64.7
Flux per m^2 (mm yr^{-1})	840	1170
Equivalent area on ground surface (m^2)	36.8	92.9

HESSD
12, 8891–8925, 2015

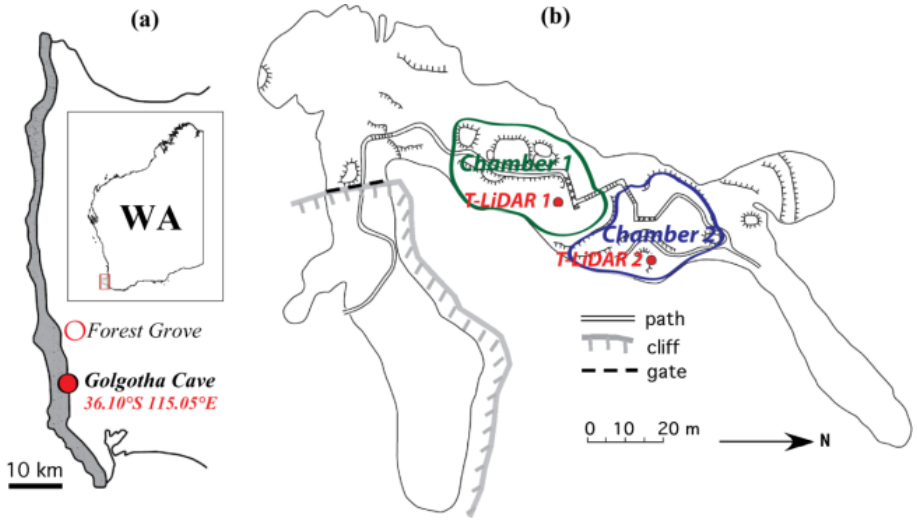

Figure 1. (a) SWWA map showing coastal belt of dune calcarenite (inset Figure indicates SWWA region). **(b)** Plan view of Golgotha cave map showing both chambers (green and blue marked areas) and T-LiDAR positions (red dots) (adapted from Mahmud et al., 2015). Chamber 1 contains sampling area 1 (T-LiDAR 1) and chamber 2 contains sampling area 2 (T-LiDAR 2) of the drip water chemistry monitoring program operating since 2005 (Treble et al., 2013, 2015).

HESSD
12, 8891–8925, 2015

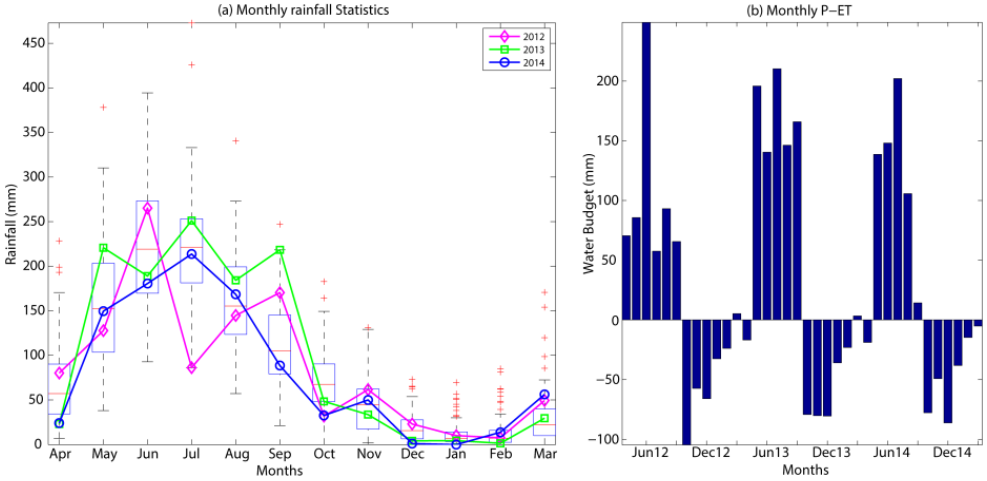

Figure 2. (a) Box plot of monthly rainfall at Golgotha cave site. **(b)** Monthly water budget for three observed hydrological years.

HESSD
12, 8891–8925, 2015

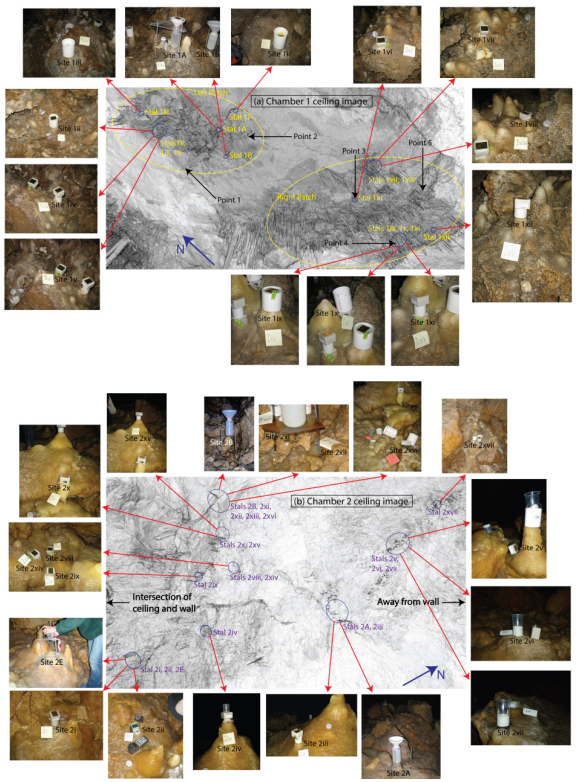

Figure 3. Both monitored ceiling images from T-LiDAR with 34 identified stalactites feeding drip loggers, **(a)** Chamber 1 and **(b)** Chamber 2. Blue circles indicate locations of the ceiling under which the loggers are placed (indicated by red arrows). The blue arrows in both figures show the geographic orientation. These ceiling stalactites locations are identified based on both on-site field observation and the alignment analysis of drip loggers and stalactites (Sect. 4.2).

HESSD
12, 8891–8925, 2015

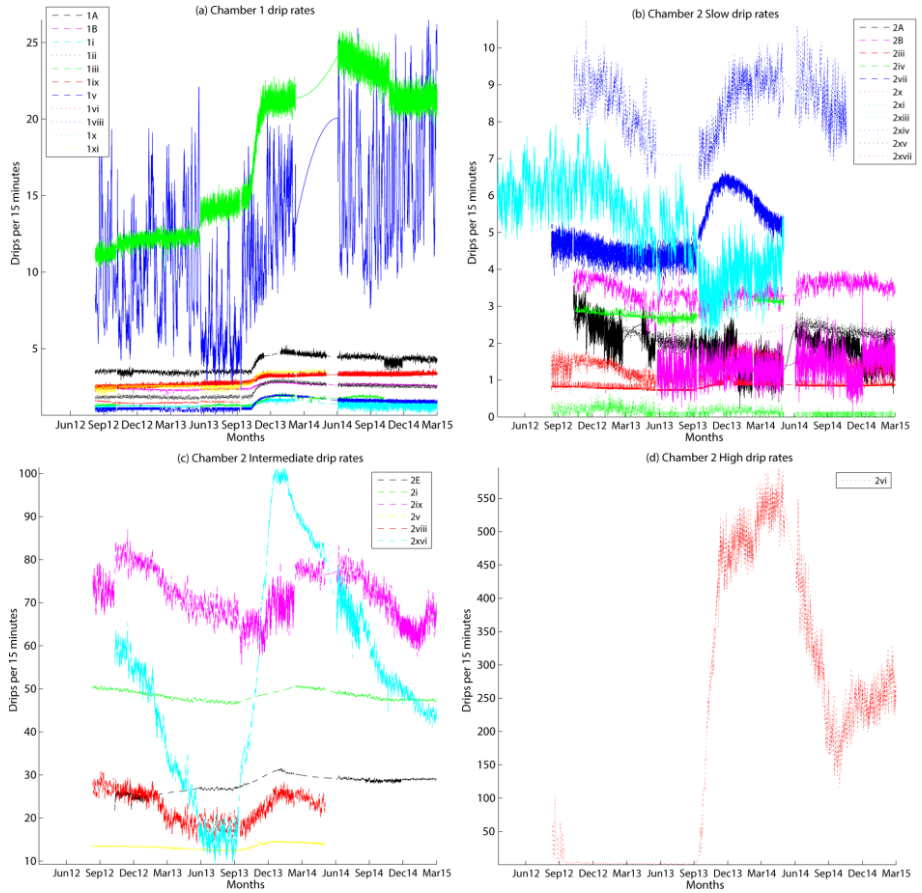

Figure 4. Both chambers' drip rate time series for the entire monitoring period. **(a)** chamber 1 drip rates. Further classification of chamber 2 drip sites for effective visualization: **(b)** slow flow rates with drip frequency of less than 10 per 15 min, **(c)** medium discharges with drip frequency between 10 to 100 per 15 min, and **(d)** fast drip rates with more than 100 drips per 15 min.

HESSD
12, 8891–8925, 2015

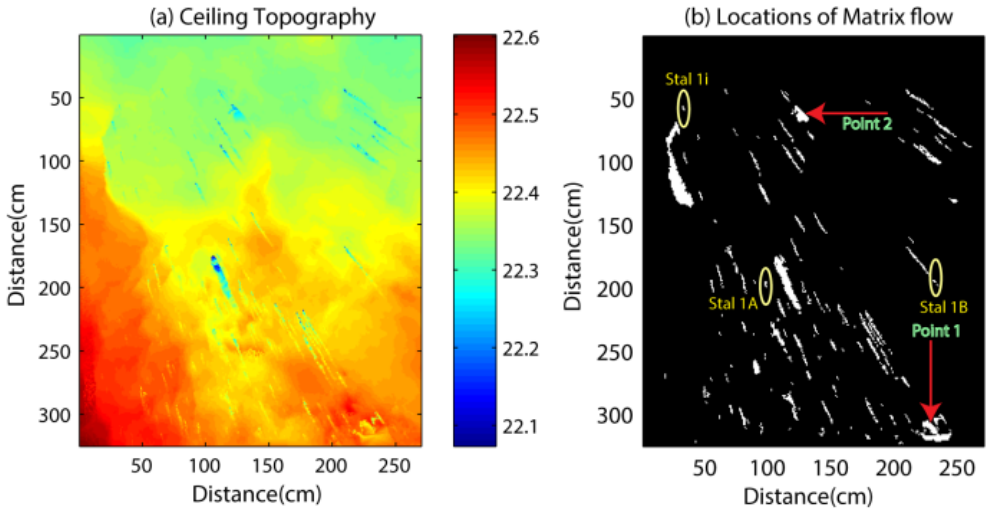

Figure 5. Morphological analysis of the cave ceiling portion consisting of Site 1A, 1B and 1i used to identify different flow patterns (icicle, soda straw, fracture and combined). **(a)** Cave ceiling topography in 2-D. Colour scales represent elevations in meters relative to the T-LiDAR receiver. Stalactites identified in **(b)** are all categorized as icicle flow pattern.

HESSD
12, 8891–8925, 2015

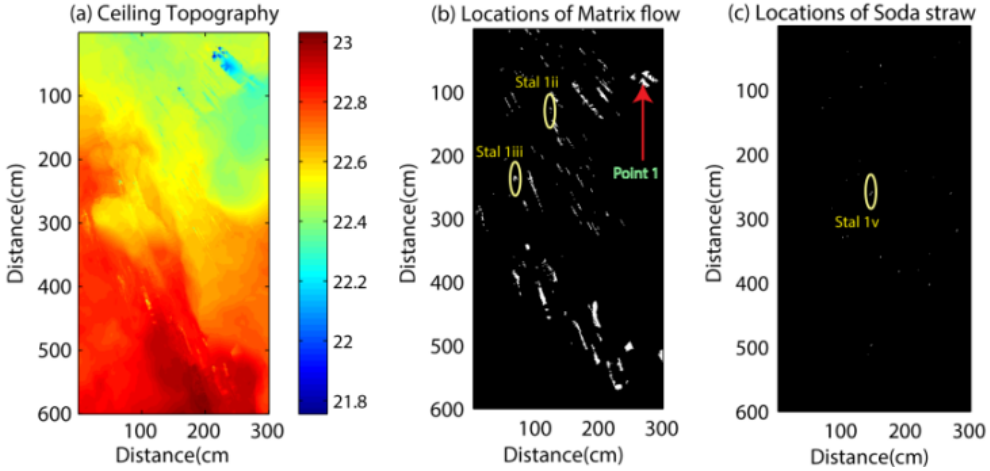

Figure 6. Morphological analysis of the cave ceiling portion consisting of site 1ii, 1iii and 1v to identify different flow patterns (icicle, soda straw, fracture and combined). **(a)** Cave ceiling topography in 2-D. Colour scales represent elevations in meters relative to the T-LiDAR receiver. **(b)** Stalactites categorized as icicle flow pattern. **(b)** Stalactite 1v categorized as soda straw.

HESSD
12, 8891–8925, 2015

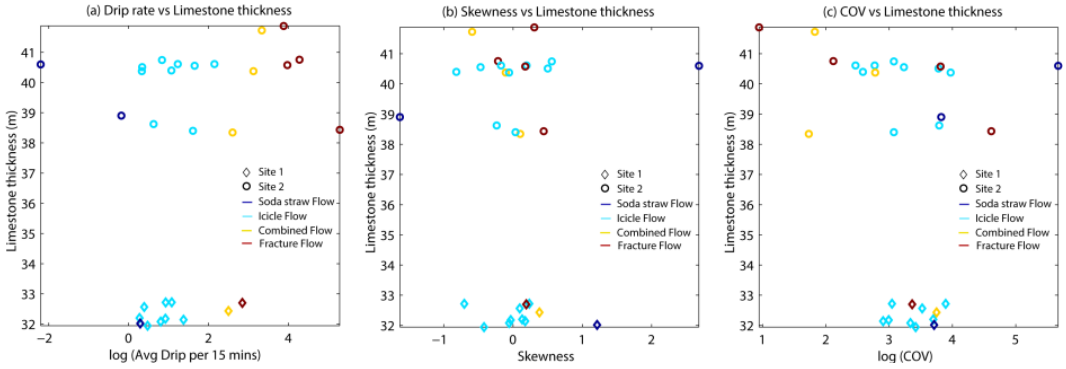

Figure 7. Drip data characteristics for different flow classifications.

HESSD
12, 8891–8925, 2015

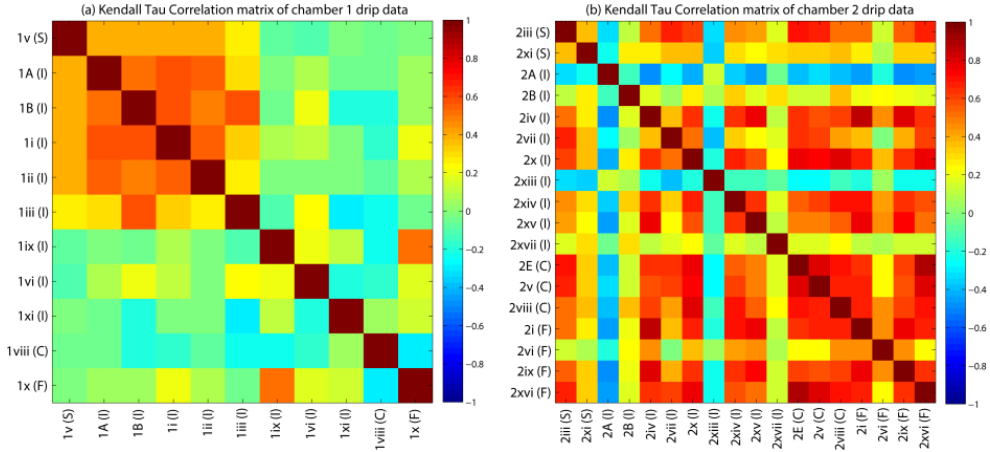

Figure 8. Correlation matrix for various drip sites with flow type classification for **(a)** Chamber 1 and **(b)** Chamber 2. Different flow types (I = Icicle, F = Fracture, C = Combined, S = Soda straw) characterized by the morphological analysis are shown in parenthesis (left *y* axes and *x* axes). Limestone thickness over the drip sites are on the right *y* axes. The colour scale indicates the correlation coefficient between drip time series.

HESSD
12, 8891–8925, 2015

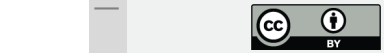

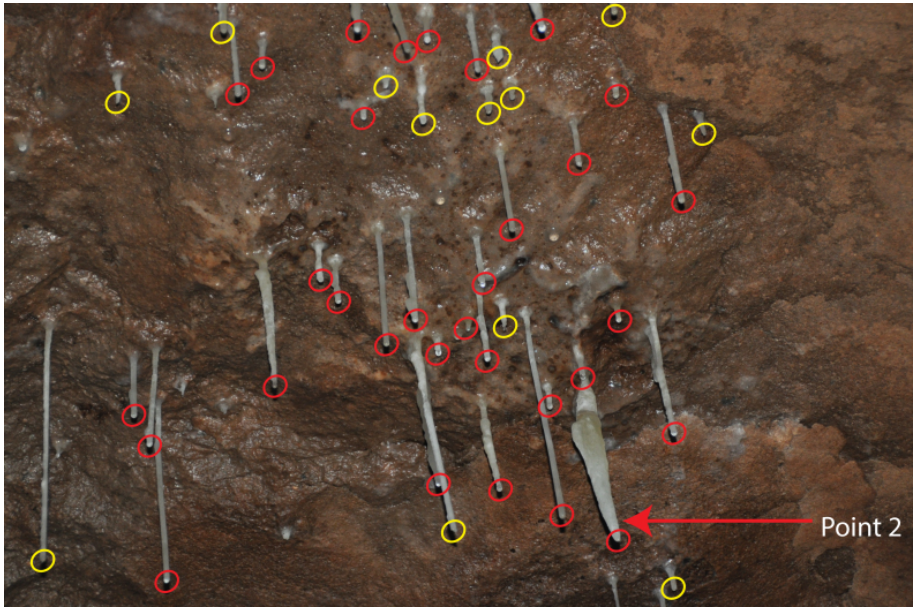

Figure 9. Actively dripping stalactite count. Red circles are stalactites identified as active in terms of dripping (displaying water droplets and/or white flashing at their tip) and yellow ones are inactive. On this photo, 32 red circles and 13 yellow ones are counted.

HESSD
12, 8891–8925, 2015

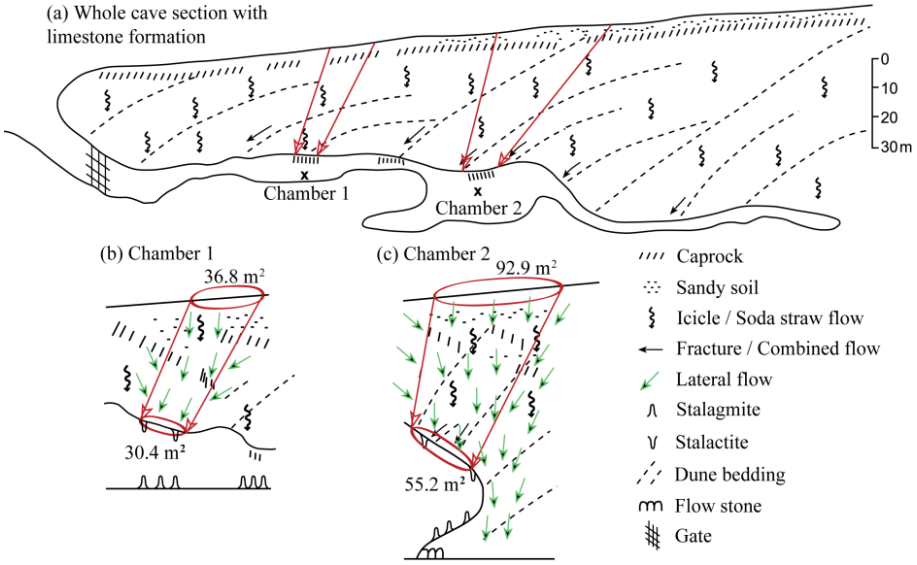

Figure 10. Representation of groundwater flow for the Tamala limestone formation in the Golgotha cave. **(a)** shows a vertical section of the entire cave with possible groundwater flows. **(b)** and **(c)** illustrate close views of chambers 1 and 2 labelling areas of ground surface infiltration and drip discharge from cave ceilings (in red circle).

HESSD
12, 8891–8925, 2015